Available online at www.sciencedirect.com
ScienceDirect
Journal of Power Sources 170 (2007) 93–100
JOURNAL OF POWER SOURCES
www.elsevier.com/locate/jpowsour

Numerical study on the compression effect of gas diffusion layer on PEMFC performance

P. Zhou, C.W. Wu *

State Key Laboratory of Structure Analysis for Industrial Equipment, Department of Engineering Mechanics, Dalian University of Technology, Dalian 116024, China

Received 28 January 2007; received in revised form 17 March 2007; accepted 29 March 2007
Available online 18 April 2007

Abstract

A numerical method is developed to study the effect of the compression deformation of the gas diffusion layer (GDL) on the performance of the proton exchange membrane fuel cell (PEMFC). The GDL compression deformation, caused by the clamping force, plays an important role in controlling the performance of PEMFC since the compression deformation affects the contact resistance, the GDL porosity distribution, and the cross-section area of the gas channel. In the present paper, finite element method (FEM) is used to first analyze the ohmic contact resistance between the bipolar plate and the GDL, the GDL deformation, and the GDL porosity distribution. Then, finite volume method is used to analyze the transport of the reactants and products. We investigate the effects of the GDL compression deformation, the ohmic contact resistivity, the air relative humidity, and the thickness of the catalyst layer (CL) on the performance of the PEMFC. The numerical results show that the fuel cell performance decreases with increasing compression deformation if the contact resistance is negligible, but an optimal compression deformation exists if the contact resistance is considerable.

Keywords: PEMFC; Contact resistance; GDL compression; Clamping force

1. Introduction

The proton exchange membrane fuel cell (PEMFC) system is considered as an alternative power source for electric vehicles by virtue of its high-energy efficiency, pollution-free characteristics, as well as the simplicity in its design and operation. It has received more and more attention in the world during the last decade. The membrane electrode assembly (MEA), consisting of a proton exchange membrane, a catalyst layer, and a gas diffusion layer, is one of the most important parts in a fuel cell system. Desirable functions of the GDL include effectively transporting the reactant gas into the catalyst layer, removing the liquid water from the catalyst layer to the gas channel, and conducting electrons with low resistance. The GDL compression deformation caused by the clamping force influences the performance of the PEMFC through changing the permeability and conductivity. The GDL material under the bipolar plate land gives a larger compression deformation than that under the channel. This inhomogeneous compression deformation may cause significant changes in the local physical properties of the GDL, such as a nonuniform porosity distribution. The interfacial contact resistance between the GDL and the bipolar plate, controlled by the clamping force, is also one of the important parameters affecting the operational voltage loss in the PEMFC. However, when the interfacial contact resistivity is very small, the contact resistance between the GDL and the land can be neglected [1].

Experimental observations show that the clamping force plays an important role in controlling the performance of PEMFC [2–4]. Lee et al. [2] measured the performances of PEMFCs with a serpentine flow field for three types of the GDLs (ELAT®, TORAY™, a combination of TORAY™ and CARBEL®) and found that the optimal clamping force depends on the GDL types. Ge et al. [3] studied the effect of the GDL compression deformation on the PEMFC performance. They designed a special test fixture of fuel cells to directly measure the compression ratio. Nitta et al. [4] concluded that the inhomogeneous compression of the GDL may lead to a significant local variation of the mass and charge transport properties.

* Corresponding author. Tel.: +86 411 84706353; fax: +86 411 84706353.
E-mail address: cwwu@dlut.edu.cn (C.W. Wu).

0378-7753/$ – see front matter © 2007 Elsevier B.V. All rights reserved.
doi:10.1016/j.jpowsour.2007.03.073

Numerical studies have been rapidly increased in order to improve the performance and cost-effectiveness of PEMFCs. Various numerical models have been developed to investigate the effect of the design and operation parameters on the PEMFC performance [5]. In our previous work [1,6], we considered the inhomogeneous compression deformation of the GDL, and studied the effects of the clamping force on the contact resistance and the performance of the fuel cell with an interdigitated flow field. The objective of our present work is to study the effects of GDL compression deformation on the performance of PEMFC with a conventional (parallel or serpentine flow pattern) flow field. We first use a finite element method (FEM) to analyze the contact pressure, the elastic deformation of the MEA, and porosity distribution. We then analyze the gas transport using a two-phase unsaturated flow model.

The numerical results show that a high compression ratio results in a lower porosity in the GDL, which will increase the transport resistance of both the gas and liquid phases. When the compression ratio is increased from 0% to 50%, the liquid water saturation in the GDL is increased by 32% and the oxygen concentration decreases by 70% under the land. On the other hand, a high compression ratio decreases the interfacial contact resistance, and hence minimizes the electrical resistance loss inside the fuel cell. These two effects may work together to yield an optimal compression ratio, depending on the properties of the gas diffusion layers and the bipolar plates. Sometimes, a negligible contact resistance occurs between the bipolar plate and the GDL. In such a case the fuel cell performance decreases with the GDL compression deformation. The influence of the GDL compression deformation on the fuel cell performance depends on the operation conditions, the GDL property and the thickness of the catalyst layer.

2. Model description

The computational domain (the region surrounded by the dashed line as shown in Fig. 1a) consists of the gas diffusion layer, the catalyst layer, the membrane, and a period of the conventional gas distributor.

2.1. FEM model

The FEM analysis model, as shown in Fig. 1b, is used to analyze the GDL elastic deformation and the porosity distribution. The deformations of the catalyst layer and the membrane are neglected due to their very larger elastic modulus than the GDL [7]. Normal displacements at the left (B6) and the right (B7) of the model, and the normal displacement at interface B3 are restricted. The bipolar plate is treated as a rigid structure. The vertical displacement of the land is given downwards, simulating the stacking process. The problem mentioned above can be described as a large deformation contact problem with the plane-strain simplicity. The plane-strain elements are used in the structure analysis and the contact elements are built at the possible contact region, as shown in Fig. 1b.

The GDL material is a carbon paper, a type of non-woven paper of carbon fibers, which can be treated as an orthotropic

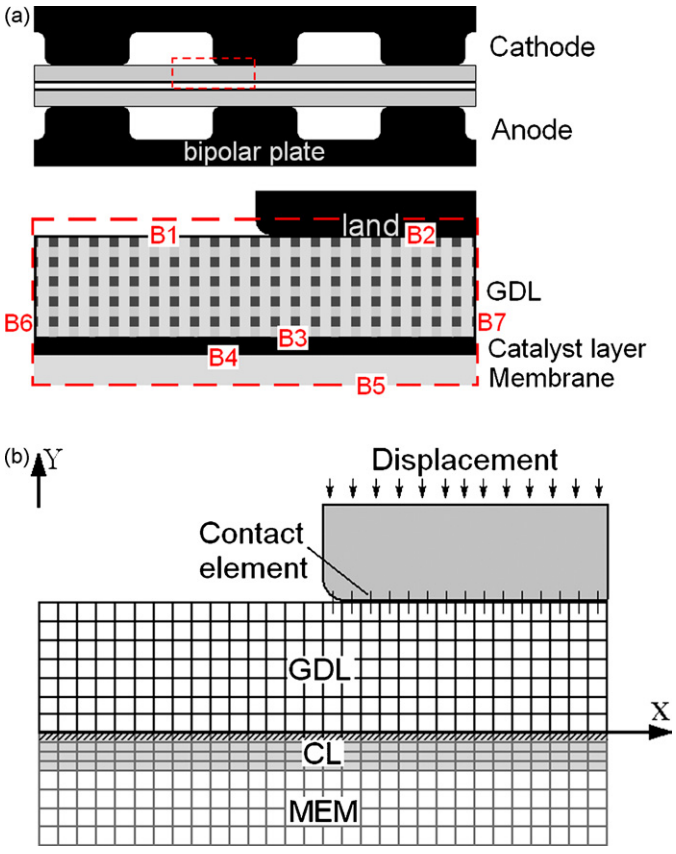

Fig. 1. Schematic diagrams of (a) PEMFC electrode and (b) FEM analysis model.

porous material. The parameters employed in the present paper are given in Table 1. The GDL elastic modulus is based on the measurements of the stress–strain relationships given by Mishra et al. [8] and Ihonen [9].

2.2. Porosity distribution and interfacial resistance calculation

The calculation methods of the porosity distribution, the GDL deformation, and the interfacial resistance have been described in details in our previous work [1]. Based on the large deformation theory of solid mechanics, the GDL porosity after stacking is

$$\phi = \frac{V_p}{V} = \frac{[V_0\phi_0 - V_0(1 - e^{\varepsilon_V})]}{V_0 e^{\varepsilon_V}} = \frac{(\phi_0 - 1 + e^{\varepsilon_V})}{e^{\varepsilon_V}} \quad (1)$$

Table 1
GDL parameters used in the FEM analysis

Initial porosity	0.78
Young's modulus, E	Through-plane: (10 MPa), in-plane: (1 GPa), References: [8,9]
Interfacial resistivity ρ (mΩ cm^2)	Case A: $\rho = 0.648(p/E_c)^{-0.7}$, Case B: $\rho = 21.74(p/E_c)^{-0.2}$, Case C: $\rho = 13.33(p/E_c)^{-1.0}$

where V_0 is the initial total volume of the porous media, ϕ_0 the initial porosity, ε_v the true bulk strain (logarithmic bulk strain), and V_p is the pore volume.

The total interfacial contact resistance in a period of the gas distributor is [1]

$$R = 2\left(\sum_{i=1}^{n} {R_i}^{-1}\right)^{-1} = 2\left(\sum_{i=1}^{n} \frac{A_i}{\rho_i}\right)^{-1} \quad (2)$$

where R_i, A_i, and ρ_i are the resistance, the contact area, and the resistivity of the ith contact element, respectively. The factor 2 in Eq. (2) is due to the same contact resistances in the anode and cathode. Three cases of the representative contact resistivity listed in Table 1 are considered in the present paper. These cases (A, B, and C) are based on the experimental observations of Mishra et al. [8], Cho et al. [10], and Davies et al. [11], for the bipolar plates made from graphite, composite material, and stainless steel, respectively. The interfacial contact resistivity increases in the order of case A < case B < case C.

2.3. Unsaturated flow model of the cathode

The present simulation is based on the two-dimensional two-phase model developed by Lin and Nguyen [12]. The basic equations and parameters, including the liquid water saturation, are developed in consideration of the dependence of the liquid water saturation on the capillary pressure. An improved two-dimensional spherical-agglomerate catalyst model [13] is used in our analysis. The following assumptions are used in the two-phase flow model of the cathode to study the effect of the clamping force on the PEMFC performance: (1) the liquid flow is steady, isothermal and laminar flow; (2) the liquid flow in the electrode is treated as a continuous phase described by Darcy's law; (3) the gas transport can be described by the diffusion mechanism; and (4) the ionic potential is set to zero at the interface of the anode catalyst layer and the membrane. Based on these assumptions, the gas species conservation equations are:

$$\nabla \cdot N_j - R_j = \nabla \cdot (-D_{\text{eff}}^{j} \nabla C_j) - R_j = 0 \quad (3)$$

where N_j is the flux of the gas species, R_j the source or sink terms, C_j the concentration of the gas species, $j = O_2$ or $j = v$ denoting oxygen or water vapor. The effective diffusion coefficient D_{eff}^{j} is

$$D_{\text{eff}}^{j} = D^j h(T) f(\phi) g(s) = D^j \left(\frac{T}{T_r}\right)^{b_1} f(\phi) g(s) \quad (4)$$

where T is the local temperature, T_r the reference temperature, $h(T)$ the temperature dependence function [14], b_1 equals 2.334 and 1.832 for vapor water and oxygen, respectively, and D^j is the diffusivity at T_r when $\phi = 1$ and $s = 0$, $f(\phi)$ and $g(s)$ are the normalized functions correlated with porosity ϕ and saturation s, respectively. Based on the work of Tomadakis and Sotirchos [16], Nam and Kaviany [15] gave:

$$f(\phi) g(s) = \phi \left(\frac{\phi - \phi_p}{1 - \phi_p}\right)^{b_2} (1 - s)^{b_3} \quad (5)$$

$\phi_p = 0.11$ is a percolation threshold, the power index b_2 is 0.521 and 0.785, and b_3 is 2 and 4, for in-plane and cross-plane diffusion, respectively. The values of these parameters are based on the numerical analysis results [15]. For the CL, a type of the packed spherical particle media, Bruggemann relation is employed:

$$f(\phi) g(s) = \phi^{1.5} (1 - s)^{1.5} \quad (6)$$

R_v is the transfer rate of water at the interface of liquid water and water vapor:

$$R_v = k_c \phi (1 - s) y_w (RT)^{-1} (P_w^{\text{sat}} - y_w P^g) q + k_v \phi s \rho_w M_w^{-1} (P_w^{\text{sat}} - y_w P^g)(1 - q) \quad (7)$$

with a switch function

$$q = \frac{1 + |y_w P^g - P_w^{\text{sat}}| / (y_w P^g - P_w^{\text{sat}})}{2} \quad (8)$$

where $y_w = C_w / C^g$, s is the saturation of the liquid water in the pore, R is the gas constant, and M_w is the molecular weight of water. When the water partial pressure ($y_w P^g$) is greater than the water saturation pressure (P_w^{sat}) the switch function $q = 1$. Otherwise, $q = 0$.

The liquid phase conservation equation is

$$\nabla \cdot N_w + R_v = 0 \quad (9)$$

where N_w is the flux of liquid water. In the CL, there is another liquid water source, $-2R_{O_2}$, due to the oxygen reduction reaction (ORR). The consumption rate of oxygen within the CL, R_{O_2}, is described by the following equation [13,17,18]:

$$R_{O_2} = \frac{C_{O_2} RT}{H} \left[\frac{1}{E_r k_{rc} (1 - \phi^{\text{cat}})} + \frac{(r_{\text{agg}} + \delta)\delta}{a_{\text{agg}} r_{\text{agg}} D^N}\right]^{-1} \quad (10)$$

Eq. (10) is based on the spherical-agglomerate model, where H is the Henry's constant, r_{agg} the agglomerate radius, a_{agg} the effective specific surface area of the agglomerate, D^N the oxygen diffusivity in the electrolyte (Nafion), k_{rc} the reaction rate constant, and E_r is the reaction effectiveness factor for spherical agglomerate. E_r is given as [19]:

$$E_r = \frac{1}{\Phi_L} \left(\frac{1}{\tanh(3\Phi_L)} - \frac{1}{3\Phi_L}\right) \quad (11)$$

where Φ_L is usually known as Thiele's modulus for chemical reactions:

$$\Phi_L = \frac{r_{\text{agg}}}{3} \sqrt{\frac{k_{rc}}{D_{\text{agg}}^{\text{eff}}}} \quad (12)$$

The effective oxygen diffusivity in the agglomerate, $D_{\text{agg}}^{\text{eff}}$, is related to the electrolyte (Nafion) fraction in the agglomerate, and is given by the following equation:

$$D_{\text{agg}}^{\text{eff}} = D^N \varepsilon_{\text{agg}}^{1.5} \quad (13)$$

where ε_{agg} is the electrolyte (Nafion) fraction in the agglomerate. The reaction rate constant is based on Butler–Volmer equation

accounting for catalyst microstructure effects [13]:

$$k_{rc} = \left(\frac{a_{Pt}^{eff}}{4F(1-\phi^{CL})}\right)\left[\frac{i_0^{ref}}{C_{O_2}^{ref}}\right] \times \left[\exp\left(-\frac{\alpha_c F}{RT}\eta\right) - \exp\left(\frac{(1-\alpha_c)F}{RT}\eta\right)\right] \quad (14)$$

where η is the local overpotential, a_{Pt}^{eff} the active or effective platinum surface area, and F is the Faraday's constant.

The transport of liquid water in the GDL and CL is driven by the capillary pressure. Based on the uniform gas pressure assumption, the flux of liquid water can be described as

$$N_w = \frac{\rho_w K_{eff}^w}{M_w \mu_w}\nabla P^c \quad (15)$$

where ρ_w is the density of the liquid water, and μ_w is the viscosity. The effective diffusion coefficient K_{eff}^w is given by

$$K_{eff}^w = K_{rl}(s)K^w \quad (16)$$

where $K_{rl}(s)$, representing the relative permeability of liquid phase [20], is proportional to the cube of the liquid water saturation, i.e.:

$$K_{rl}(s) = s^3 \quad (17)$$

K^w is the absolute permeability of water. Kozeny–Carman relation is used to calculate the absolute permeability when the porosity is changed. Based on the constant Kozeny–Carman coefficient, one has:

$$K^w = K_0^w \frac{\phi^3(1-\phi_0)^2}{\phi_0^3(1-\phi)^2} \quad (18)$$

where ϕ_0 and K_0^w are the initial porosity and the absolute permeability, respectively. The capillary pressure is related to the liquid water saturation via a Leverette function $J(s)$ [21]:

$$P^c = \sigma\cos(\theta_c)\left(\frac{\phi}{K^w}\right)^{1/2} J(s),$$

$$J(s) = \begin{cases} 1.417s - 2.120s^2 + 1.263s^3, & \text{if } \theta_c > 90^\circ \\ 1.417(1-s) - 2.120(1-s)^2 + 1.263(1-s)^3, & \text{if } \theta_c < 90^\circ \end{cases} \quad (19)$$

where σ is the surface tension of liquid water and air system, and θ_c is the contact angle of water on the GDL.

The liquid water transport in the membrane is driven by the water concentration gradient and electro-osmotic drag:

$$N_w = \frac{i_+}{F}n_d - D_w^N \nabla C_w^N \quad (20)$$

where C_w^N is the liquid water concentration in the membrane. The net electro-osmotic drag coefficient, n_d, and the diffusivity of the liquid water, D_w^N, in the membrane are the functions of the water content in the membrane:

$$D_w^N = 10^{-6}e^{2416(1/303-1/T)}(2.563 - 0.33\lambda + 0.0264\lambda^2 - 0.000671\lambda^3) \quad (21)$$

$$n_d = \frac{2.5}{22}\lambda = \frac{2.5}{22}\frac{C_w^N}{C_f} \quad (22)$$

where C_f is the concentration of the fixed charge sites in the membrane. At interfaces B4 and B5, C_w^N is related to the water vapor activity α [12] and can be described as

$$\text{if } s = 0, \quad C_w^N = C_f(0.043 + 17.81\alpha - 39.85\alpha^2 + 36.0\alpha^3),$$
$$\text{if } s > 0, \quad C_w^N = 14C_f + 2.8C_f s \quad (23)$$

2.4. Charge transport

The local overpotential η can be described by the following equation:

$$\eta = \Phi_e - \Phi_+ - U \quad (24)$$

where U is the reference electrode potential, Φ_e is the electron potential, and Φ_+ is the ion potential. The potentials of electron and ion can be obtained through the following charge conservation equation:

$$\nabla \cdot i_{+(e)} = \nabla \cdot (-\kappa_{+(e),eff}\nabla\Phi_{+(e)}) = R_{+(e)} \quad (25)$$

The effective conductivities of the catalyst layer for ion, $\kappa_{+,eff}$, and electron, $\kappa_{e,eff}$, are described as

$$\kappa_{+,eff} = \kappa_+^N[(1-\phi^{CL})\varepsilon_{agg}]^{1.5}$$
$$\kappa_{e,eff} = \kappa_e^C[(1-\phi^{CL})(1-\varepsilon_{agg})]^{1.5} \quad (26)$$

where κ_+^N is the ionic conductivity of the membrane, and κ_e^C is the electronic conductivity of the carbon black in agglomerate. The source/sink terms of electron and ion existing in the CL are given as

$$R_+ = R_e = 4FRO_2. \quad (27)$$

2.5. Boundary condition

There are seven boundaries or interfaces within the studied domain as shown in Fig. 1. The boundary conditions are listed in Table 2. At the interface of the GDL and the CL (B3), the properties of the two layers cause a discontinuity of the liquid saturation. The continuity assumption of the capillary pressure at the interface of the two layers is used for hydrophobic GDL:

$$\cos(\theta_c^{GDL})\left(\frac{\phi^{GDL}}{K^{GDL}}\right)^{1/2} J(s^{GDL}) = \cos(\theta_c^{CL})\left(\frac{\phi^{CL}}{K^{CL}}\right)^{1/2} J(s^{CL}) \quad (28)$$

Eq. (28) is inapplicable for hydrophilic GDL. In such a case we assume that $s^{CL} = 0$ at interface B3.

2.6. Solution procedure

The equations together with the boundary conditions listed in Table 2 and described in the previous sections are solved with the finite element method and the finite volume method. The code is designed using Fortran Language. The studied domain is divided

Table 2
The boundary conditions in the numerical analysis [12]

Interface	Variables				
	C_j (j: O_2 or vapor)	s	Φ_+	Φ_e	C_w^N
B1	$C_j = C_j^{in}$	$s = s^{in}$	N/A	$i_e\|_y^{GDL} = 0$	N/A
B2	$N_j\|_y^{GDL} = 0$	$N_w\|_y^{GDL} = 0$	N/A	$\Phi_e = U$	N/A
B3	$N_j\|_y^{GDL} = N_j\|_y^{CL}$	$N_w\|_y^{GDL} = N_w\|_y^{CL}$	$i_+\|_y^{CL} = 0$	$i_e\|_y^{GDL} = i_e\|_y^{CL}$	$\partial C_w^N/\partial y = 0$
B4	$N_j\|_y^{CL} = 0$	$N_w\|_y^{CL} = N_w\|_y^{mem}$	$i_+\|_y^{CL} = i_+\|_y^{mem}$	$i_e\|_y^{CL} = 0$	$C_w^N = C_w^N(\alpha^{CL}, s)$
B5	N/A	N/A	N/A	N/A	$C_w^N = C_w^N(\alpha^{anode})$
B6 and B7	$\partial C_j/\partial x = 0$	$\partial s/\partial x = 0$	$\partial \Phi_+/\partial x = 0$	$\partial \Phi_e/\partial x = 0$	$\partial C_w^N/\partial x = 0$

into rectangle elements with four nodes. Finite element analysis for the elastic deformation of the GDL is first carried out to obtain the real shape of the GDL after deformation. The grid is then changed into the approximate orthogonal curvilinear grid. Based on this new grid, finite volume method is used to analyze the distributions of the reactants and products. The parameters used in the calculation are listed in Table 3.

3. Results and discussions

Generally speaking, the output voltage and power density of a fuel cell will decrease with increasing the compression due to the decrease of the GDL porosity. However, a contrary phenomenon is sometimes observed in the low compression region [2,3]. The main reason why the performance of PEMFC increases with the compression is that the bulk resistivity of the GDL and the interfacial contact resistance decrease with the compression deformation of the GDL. The total interfacial contact resistance includes those coming from the bipolar plate/GDL interface, the GDL/CL interface, and the CL/membrane interface. However, the possible contact resistance occurring at the GDL/CL interface and the CL/membrane interface is considered to be negligible when compared with the plate/GDL interface resistance.

Fig. 2 gives the numerical results with the three cases of the interfacial resistivity as described in Table 1. When the compression displacement of the GDL is fixed at 0.0185 mm, the contact resistances for cases A, B, and C are 48.8 mΩ cm, 667 mΩ cm and 1648 mΩ cm, respectively. There is a considerable influence

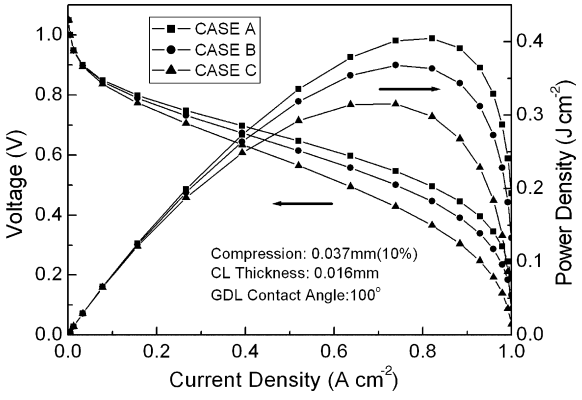

Fig. 2. Polarization curves for the contact resistivity described by three different equations.

of the contact resistance on the output voltage and power density of the fuel cell. It can be inferred that the contact resistance mainly affects the slope of the polarization curve at the ohmic region.

Fig. 3 shows the polarization curves at different compression ratios for case C. The compression ratio is defined as the

Table 3
The physical properties of MEA and employed parameters in the calculations

Parameter	Value
Gas diffusion layer properties	
Channel width (half)	0.05 cm
Shoulder width (half)	0.05 cm
Initial porosity (Toray 120), ϕ_0^{GDL}	0.78
Initial thickness (Toray 120), h_0^{GDL}	0.037 cm
Absolute permeability, K_{GDL} [22]	8.69×10^{-8} cm^2
Contact angle, θ_c^{GDL} [23]	100°; 89°
Electronic conductivity κ_e^{GDL}	
In plane (Toray 120)	213 S cm^{-1}
Through plane (Toray 120)	12.5 S cm^{-1}
Catalyst layer properties	
Initial porosity, ϕ_0^{CL} [13]	0.1
Initial thickness, h_0^{CL}	0.0016 cm; 0.003 cm
Absolute permeability, K_{CL}	10^{-11} cm^2
Contact angle, θ_c^{CL}	110°
Effective platinum surface area, a_{Pt}^{eff} [13]	303797.5 cm^2 cm^{-3}
Electrolyte fraction in agglomerate, ε_{agg} [24]	0.5
Carbon black conductivity [12]	100 S cm^{-1}
Henry's constant, H [25]	0.3125 atm m^3 mol^{-1}
Ref. O_2 concentration, $C_{O_2}^{ref}$ [26]	0.85 mol m^{-3}
Membrane properties	
Initial thickness, h_0^{mem}	0.012 cm
Ionic conductivity, κ_i^{mem}	0.1 S cm^{-1}
Operation conditions	
Temperature, T	65 °C
Cathode gas pressure	1 atm
Mole fraction of oxygen in the air inlet	0.21
Humidity in the air inlet	75%; 100%
Humidity at anode	100%
Water saturation level at channel	0
Evaporation rate constant, k_v	100 atm^{-1} s^{-1}
Condensation rate constant, k_c	100 mol atm^{-1} s^{-1} cm^{-3}
Cathode transfer coefficient, α_c [26]	1 (≥0.8 V)
	0.61 (<0.8 V)
Reference exchange current density, i_0^{ref} [26]	3.85×10^{-8} A cm^{-2} (≥0.8 V)
	1.5×10^{-6} A cm^{-2} (<0.8 V)
Reference electrode potential, U	1.1 V

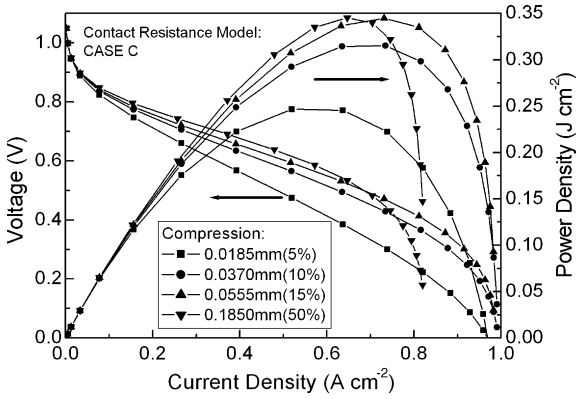

Fig. 3. Polarization curves for several compression ratios as indicated.

ratio of the normal compression displacement to the initial GDL thickness. We find that the voltage increases with increasing compression due to the decrease in the ohmic overpotential. It is shown that there exists an optimal compression displacement (∼0.0555 mm). The limiting current decreases with an increase in the GDL compression deformation.

The dependence of the limiting current on the transport ability of the reactant gas varies with the porosity and the liquid water distribution. Fig. 4 shows the polarization curves with different cathode air humidities in order to study the influence of liquid water saturation. With the decrease in the relative humidity, the saturation of liquid water also decreases due to the interfacial transfer of water between the liquid water and the water vapor. When the relative humidity is decreased to ∼75%, the liquid water saturation in most of the regions of the GDL deceases to about null. From Fig. 4, it is shown that the higher the humidity, the lower the limiting current and the greater the compression effect.

There is a significant effect of the liquid water saturation on the PEMFC performance. The saturation of liquid water is affected by the GDL wettability. Gurau et al. [23] have studied the internal contact angle of water within the GDL material. It is estimated to be 89° for 30% PTFE and 100° for 70% PTFE. Comparing what is shown in Figs. 4 and 5, it is found that the limiting current of the fuel cell decreases from ∼0.98 A cm^2 to ∼0.66 A cm^2 for 15% of the compression ratio when the contact angle decreases from 100° to 89°. The effect of the compression

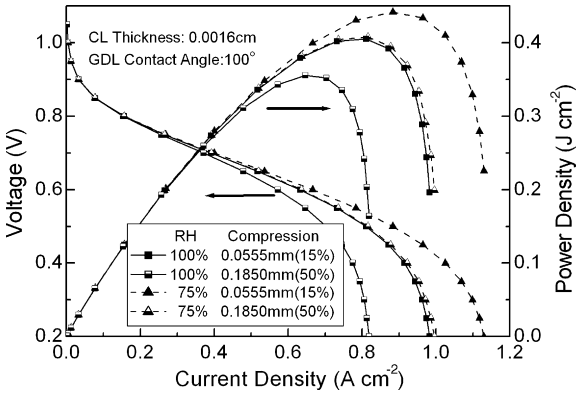

Fig. 4. Polarization curves with different cathode air humidities.

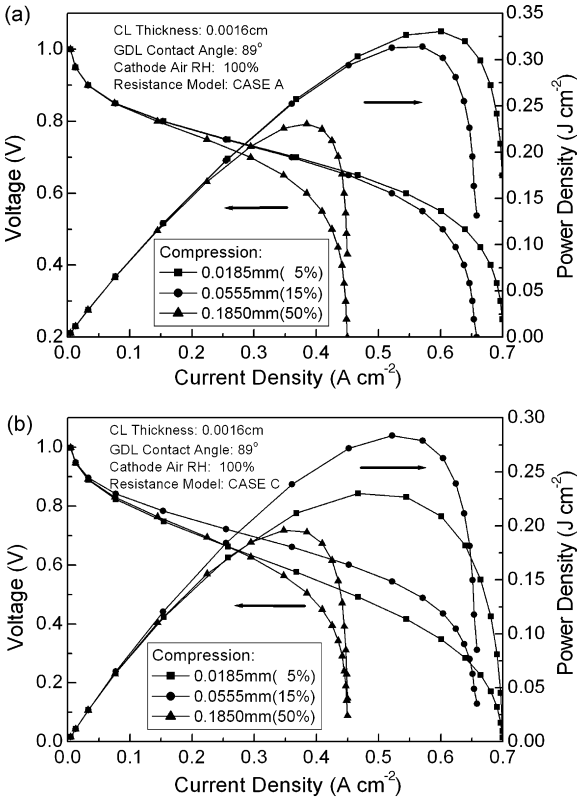

Fig. 5. Polarization curves for different compressions and different contact resistivity models: (a) contact resistivity described by case A and (b) contact resistivity described by case C.

on the fuel cell performance is greater when the contact angle is 89° than when the contact angle is 100°. Comparing what is shown in Figs. 5a and b, the limiting current density decreases with increasing compression. However, there exists an optimal compression ratio to give the highest power density when case C is used. But no apparent optimal compression ratio is found for case A. Generally speaking, there always exists an optimal compression ratio for a practical FEMFC system because the interfacial contact resistivity approaches infinite when the compression ratio is close to zero (zero interfacial pressure). For case A, the optimal compression ratio may range from 0 to 5%. The experimental measurements of Ge et al. [3] show that the fuel cell performance decreases with an increase in the compression ratio when the compression ratio ranges from 15% to 45%. However, it is estimated that the optimal compression ratio may be between 0% and 15%, which was not be found in their experiments.

The GDL compression always decreases the porosity, thus reducing the transport ability of the reactant gas and liquid water in the GDL. Fig. 6 shows the distribution of the mole fraction of oxygen within the GDL and CL and the distribution of the liquid water saturation within the GDL when the compression of the GDL is set at 0% and 50%. A higher water saturation may exist in the GDL when the compression ratio is 50% due to the reduced porosity. From Fig. 6b and Fig. 6d, the maximum liquid water saturation is 0.489 and 0.647 when the compression ratio is set at 0% and 50%, respectively. It is difficult to transport

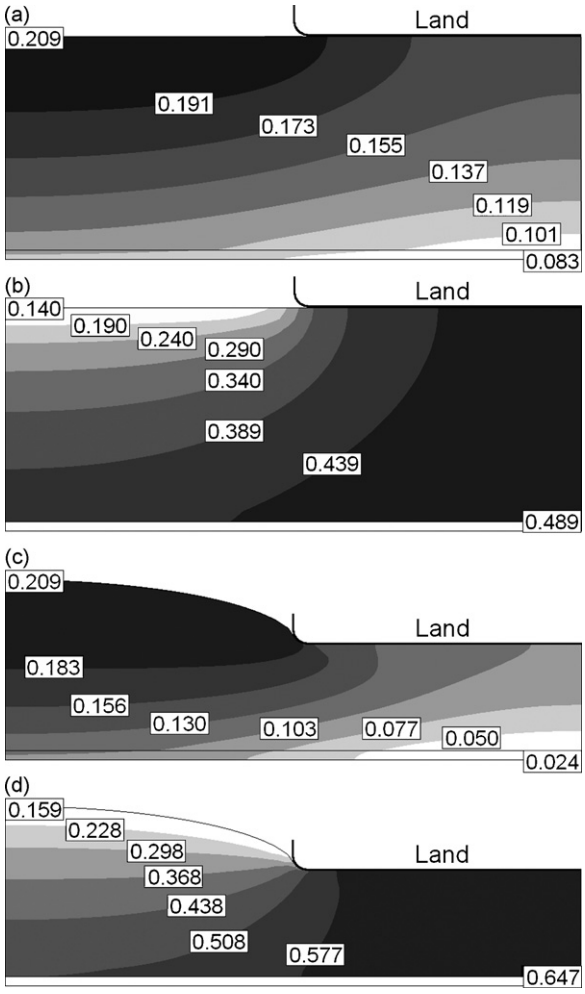

Fig. 6. Distributions of (a) oxygen mole fraction with 0% compression ratio, (b) liquid water saturation level with 0% compression ratio, (c) oxygen mole fraction with 50% compression ratio and (d) liquid water saturation level with 50% compression ratio (cell voltage: 0.3 V; contact angle of the GDL: 89°; contact resistance: neglected).

oxygen from the channel/GDL interface to the CL due to the reduced effective void for the gas diffusion. When the compression ratio increases from 0% to 50%, the oxygen concentration decreases by about 70% under the land. In this paper, we use a given boundary condition at the channel/GDL interface for the liquid water saturation and the gas components. However, the GDL compression affects the cross-section area of the channel which affects the removal of the liquid water and the gas near the channel/GDL interface. When the compression ratio reaches 25% and 50%, the GDL surface goes into the channel by about 0.0552 mm and 0.1115 mm, respectively, due to its elastic deformation. The influence of the cross-section area of the channel on the performance of the PEMFC can be studied in a three-dimensional flow field analysis.

Finally, we study the combined effects of the CL thickness and GDL contact angle on the performance of the fuel cell as shown in Fig. 7a and Fig. 7b. Usually, a larger CL thickness gives a higher limiting current and a more significant effect of the compression on the performance, especially when the GDL contact angle is 89°.

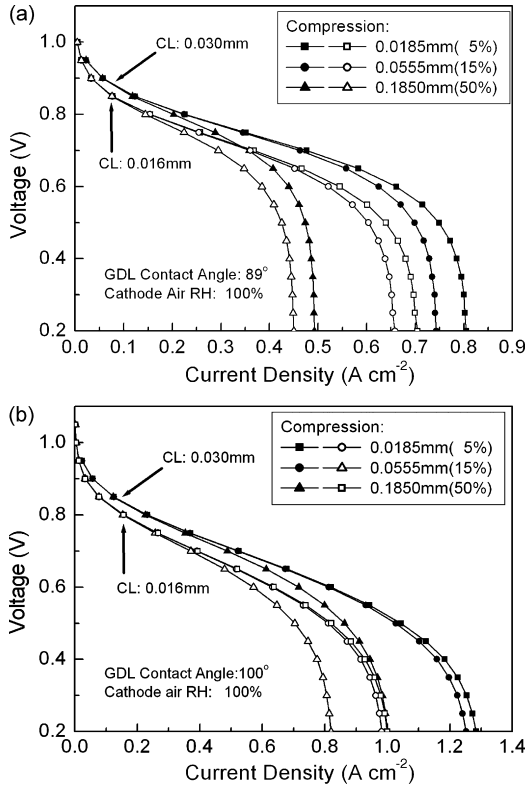

Fig. 7. Polarization curves at different compressions and CL thickness: (a) the contact angle is 89° and (b) the contact angle is 100°.

What is shown above can explain both of the experimental observations given by Lee et al. [2] and Ge et al. [3]. However, the effect of the compression on the fuel cell performance in the present simulation is slightly smaller than what was measured by Ge et al. [3]. One possible reason for this may be that the effects of compression on the physical and geometrical properties of the membrane and catalyst layers were not considered in the present simulation. Furthermore, the GDL compression will also affect the anode flow field. This may cause some difference between the experiments and the numerical simulation. It should be stressed that the contact resistivity depends on not only the land conduction property but also the GDL conduction property. That is why Lee et al. [2] obtained different results for different GDLs in their experiments.

4. Conclusions

In order to study the effect of the GDL compression deformation on the PEMFC performance, a simulation method is developed in the present paper. Finite element method (FEM) and two-phase flow model are used to investigate the polarization curves of the PEMFC when the GDL deformation in the cathode with the conventional flow field is considered. We have studied the combined effects of the compression ratio, the interfacial contact resistivity, the CL thickness, the GDL wettability, and the air relative humidity. From the numerical results, we have reached the following conclusions:

(1) The GDL compression deformation decreases the contact resistance, which in turn causes a drop in the ohmic overpotential of the polarization curve, especially for case B and case C (high interfacial contact resistivity). Until now, most of the experimental observations for the contact resistivity are higher than what is described by case B. Therefore, the contact resistance plays an important role in polarization curve simulation.
(2) Large GDL compression deformation and large porosity variation reduce the transport ability of the reactant gas and liquid water in the GDL. On the other hand, the GDL compression deformation reduces the ohmic overpotential. The optimal compression ratio results from the combined effects of the GDL compression deformation on the contact resistance and the mass transfer.
(3) The effect of the GDL compression deformation is considerable large in the case of high current density, high air humidity, and thick catalyst layer due to the increasing liquid water saturation.

Acknowledgments

The authors would like to thank Mr. Higier and Prof. Hongtan Liu at the University of Miami for their helpful discussions. This work was supported by the NSFC (10421002, 10332010), National Basic Research Program of China (2006CB601205), and the Science Research Foundation of Liaoning Province, China (20052178).

References

[1] P. Zhou, C.W. Wu, G.J. Ma, J. Power Sources 163 (2007) 874–881.
[2] W.K. Lee, C.H. Ho, J.W. Van Zee, M. Murthy, J. Power Sources 84 (1999) 45–51.
[3] J.B. Ge, A. Higier, H.T. Liu, J. Power Sources 159 (2006) 922–927.
[4] I. Nitta, et al., J. Power Sources (2006), doi:10.1016/j.jpowsour.2006.11.018.
[5] A.Z. Weber, J. Newman, Chem. Rev. 104 (2004) 4679–4726.
[6] P. Zhou, C.W. Wu, G.J. Ma, J. Power Sources 159 (2006) 1115–1122.
[7] Y. Tang, A.M. Karlsson, M.H. Santare, M. Gilbert, S. Cleghorn, W.B. Johnson, Mater. Sci. Eng. A 425 (2006) 297–304.
[8] V. Mishra, F. Yang, R. Pitchumani, J. Fuel Cell Sci. Technol. 1 (2004) 2–9.
[9] J. Ihonen, Development of Characterisation Methods for the Components of the Polymer Electrolyte Fuel Cell, Ph.D. Thesis, Department of Chemical Engineering and Technology Applied Electrochemistry Kungliga Tekniska Högskolan Stockholm, 2003, pp. 40.
[10] E.A. Cho, U.-S. Jeon, H.Y. Ha, S.-A. Hong, I.-H. Oh, J. Power Sources 125 (2004) 178–182.
[11] D.P. Davies, P.L. Adcock, M. Turpin, S.J. Rowen, J. Power Sources 86 (2000) 237–242.
[12] G. Lin, T.V. Nguyen, J. Electrochem. Soc. 153 (2006) A372–A382.
[13] W. Sun, B.A. Peppley, K. Karan, Electrochim. Acta 50 (2005) 3359–3374.
[14] R.B. Bird, W.E. Stewart, E.N. Lightfoot, Transport Phenomena, John Wiley & Sons, New York, 1960.
[15] J.H. Nam, M. Kaviany, Int. J. Heat Mass Transfer 46 (2003) 4595–4611.
[16] M.M. Tomadakis, S.V. Sotirchos, AIChE J. 39 (1993) 397–412.
[17] K. Broka, P. Ekdunge, J. Appl. Electrochem. 27 (1997) 281–289.
[18] N.P. Siegel, M.W. Ellis, D.J. Nelson, M.R. von Spakovsky, J. Power Sources 115 (2003) 81–89.
[19] H.S. Fogler, Elements of Chemical Reaction Engineering, Prentice-Hall, New Jersey, 1999.
[20] U. Pasaogullari, C.Y. Wang, Electrochim. Acta 49 (2004) 4359–4369.
[21] U. Pasaogullari, C.Y. Wang, J. Electrochem. Soc. 151 (2004) A399–A406.
[22] M.V. Williams, H.R. Kunz, J.M. Fenton, J. Electrochem. Soc. 151 (2004) A1617–A1627.
[23] V. Gurau, M.J. Bluemle, E.S. De Castro, Y.-M. Tsou, J.A. Mann Jr., T.A. Zawodzinski Jr., J. Power Sources 160 (2006) 1156–1162.
[24] A.A. Kulikovsky, J. Appl. Electrochem. 30 (2000) 1005–1014.
[25] A. Parthasarathy, S. Srinivasan, A.J. Appleby, C.R. Martin, J. Electrochem. Soc. 139 (1992) 2856–2862.
[26] A. Parthasarathy, S. Srinivasan, A.J. Appleby, C.R. Martin, J. Electrochem. Soc. 139 (1992) 2530–2537.